

ORGANISATION OF VELOCITY STRUCTURES ASSOCIATED WITH LARGE PASSIVE SCALAR GRADIENTS IN A TURBULENT BOUNDARY LAYER.

Angeliki Laskari

Graduate Aerospace Laboratories
California Institute of Technology
Pasadena, California 91125, USA
alaska@caltech.edu

Theresa Saxton-Fox

Department of Aerospace Engineering
University of Illinois at Urbana-Champaign
Urbana, IL 61801, USA
tsaxtonf@illinois.edu

Beverley McKeon

Graduate Aerospace Laboratories
California Institute of Technology
Pasadena, California 91125, USA
mckeon@caltech.edu

ABSTRACT

Planar particle image velocimetry (PIV) measurements were performed in a thermal boundary layer with simultaneous measurements of the streamwise density gradient, averaged across the boundary layer height. Previous work on the topic (Saxton-Fox *et al.*, 2019) revealed that large density gradients were associated with tall wall-normal velocity structures extending across the entire boundary layer height. The authors suggested that these structures were a result of a wall-normal average of smaller scales, which reside at different locations from the wall, and contribute to the same density gradient change. Results from the present work support this model and show that, if a second condition on the vertical location of the identified features is imposed, one can extract wall-normal velocity structures that are localized in the vertical direction. Their average wall-normal extent is found to be around 0.1δ , with no significant variation across the boundary layer height. The corresponding conditionally averaged streamwise velocity fluctuations also show a change in sign from the wall up to edge of the boundary layer, consistent with the underlying density gradient condition. This sign change is found to originate on average from upstream leaning structures of opposite signs, while the inferred flow topology is shown to agree with earlier results on the topic (Antonia and Fulachier, 1989).

INTRODUCTION

Knowledge of the scalar transport mechanism in turbulent flows is essential for many industrial and environmental applications, due to its direct implications on mixing, reaction dynamics, and pollutant dispersion. In the case of a mildly heated boundary layer, where temperature acts as a passive scalar, and the Prandtl number is near unity, temperature and momentum transport are in close correspondence (Antonia *et al.*, 2009) and therefore knowledge of the velocity field can be leveraged to infer conclusions about the scalar field and vice-versa. Specifically regarding the latter, passive scalar contaminants have been used for many decades to study coherent structures in wall-bounded flows (Chen

and Blackwelder, 1978; Bisset *et al.*, 1991, among others), while the mechanism of scalar mixing and its link to velocity structures have been also examined (see for example Fulachier and Dumas, 1976; Antonia *et al.*, 2009; Abe *et al.*, 2009).

When the full scalar field is not readily available (which is most often the case, especially in experimental studies), measurements of scalar gradients can still provide vital information on velocity structures. Such an alternative, when the scalar contaminant is temperature, was used by Saxton-Fox *et al.* (2019), who employed a Malley probe set-up (MP) to acquire integral measurements of streamwise density gradients in a mildly heated subsonic boundary layer following work in the field of aero-optics (Malley *et al.*, 1992; Gordeyev *et al.*, 2014, for compressible flows). Simultaneous PIV measurements allowed for the identification of velocity structures conditioned on large density gradients; tall vertical velocity structures on either side of the MP beam, of opposing signs, spanning the boundary layer height, were found to be associated with large streamwise density gradients (Saxton-Fox *et al.*, 2019). The authors postulated that these structures were a result of a wall-normal average of instantaneous smaller scales residing at the same streamwise location but at different heights y from the wall, depending on the phase of large-scale streamwise velocity structures. In this work we assess the proposed model. We attempt to separate the different wall-normal velocity scales triggering large deflections of the optical beam (and therefore large density gradients), and determine their wall-normal extent while also identifying the localised signatures of the corresponding streamwise velocity fluctuations.

EXPERIMENTAL SET-UP

Throughout this paper, we use the coordinate system x , y , and z to denote the streamwise, wall-normal and spanwise directions, respectively and u , v , w to denote the corresponding velocity components. Concurrent planar PIV and aero-optic measurements were performed in a moderately

heated turbulent boundary layer in the Merrill recirculating wind tunnel located at the California Institute of Technology. The test section is 2.1 m long with a square cross-section spanning $0.6 \text{ m} \times 0.6 \text{ m}$ in y and z , respectively. The boundary layer was developed on an aluminium flat plate, tripped at the leading edge. Two sections of the plate were heated with rubber resistance heaters, their temperature kept at 22°C above the freestream temperature. The Prandtl number was $Pr = 0.71$, while mean flow and turbulence statistics between heated and unheated conditions were identical, indicating that temperature acted as a passive scalar. Measurements were acquired downstream of the two heated plates, at a distance 1.9 m downstream of the trip.

For the aero-optic measurements, a Malley probe (MP) setup (Malley *et al.*, 1992; Gordeyev *et al.*, 2015; Saxton-Fox *et al.*, 2019) was used to acquire streamwise density gradients, at the same streamwise–wall-normal plane as the PIV measurements. This was achieved by recording the streamwise position of a laser beam, passing twice through the thermal boundary layer, after being spatially filtered. The beam’s position was recorded at 32 kHz and high-pass filtered at 100 Hz to remove low-frequency noise, using a Butterworth filter. The addition of heat in the flow led to a continuously varying density field, $\rho(x, y, z, t)$, directly proportional to the index of refraction change: $n(x, y, z, t) = 1 + K_{GD}\rho(x, y, z, t)$, where K_{GD} is the Gladstone-Dale constant (Gladstone and Dale, 1862). This change in refractive index distorted the incoming wave-front (Gordeyev *et al.*, 2015) and the time-varying fluctuation of the beam’s recorded position could then be used to estimate the final deflection angle of the beam, $\theta(t)$, an integral measurement of the distortion across the entire boundary layer height. This can be related to the streamwise density gradient (Saxton-Fox and McKeon, 2017, equation 1):

$$\theta(y_f, t) - \theta(y_i) \approx \frac{K_{GD}}{1 + K_{GD}\rho_a} \int_{y_i}^{y_f} \frac{\partial \rho}{\partial x}(x_0, y, z_0, t) dy, \quad (1)$$

where $\theta(y_i)$ and $\theta(y_f, t)$ are the initial and final angles of the incoming beam respectively, ρ_a the ambient density of the fluid, and x_0, z_0 the streamwise–spanwise coordinates of the beam location. This means that, for a beam entering the flow at a zero angle, $\theta(y_i) = 0$, a negative exit angle, $\theta(y_f)$, corresponding to a negative streamwise gradient, will indicate an upstream deflection of the beam (x positive downstream, figure 1). Considering only a single step change in density across y , such a deflection can result from a density interface inclined either upstream or downstream (figure 1). A similar behaviour can be expected from the streamwise velocity fluctuations, given the well documented similarity between streamwise velocity and passive scalar fluctuations fields (Antonia *et al.*, 2009 among others).

For the PIV measurements, Diocetyl—di(2-ethylhexyl)—sebacate liquid was used for the seeding, atomised with a LaVision Aerosol Generator into particles with a nominal diameter $d_p = 0.25 \mu\text{m}$. The particles were illuminated with a YLF Photonics laser (DM20-527), running in double pulse mode, with a pulse separation $dt = 38 \mu\text{s}$. Images were recorded using a Phantom Miro 320S high-speed camera (1920×1080 pixels), fitted with a Tamron f/3.5 SP AF Macro lens with a focal length of 180 mm at an aperture stop of f/8. The system was synchronised

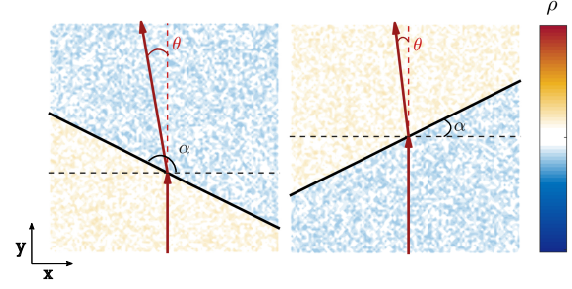


Figure 1. Beam deflection schematic for a negative streamwise density gradient event, $\frac{\partial \rho}{\partial x} < 0$ assuming a step change in density and index of refraction. The beam experiences an upstream deflection regardless of the angle α , between the density front and the horizontal. Upstream leaning density front, $\frac{\partial \rho}{\partial x} < 0$, $\alpha < \pi/2$ (left), downstream leaning density front, $\frac{\partial \rho}{\partial x} > 0$, $\alpha > \pi/2$ (right).

using a LaVision high-speed controller. The camera captured a field of view (FOV) approximately $0.05 \text{ m} \times 0.04 \text{ m}$ ($1.5\delta \times 1.0\delta$), in x and y respectively, at 600 Hz, with a resulting digital resolution of 29 pix/mm. We acquired 19,287 images using DaVis 8.3.1, which we subsequently processed using the same software applying an iterative correlation with a final interrogation window of 32×32 pixels with an overlap factor of 50%. The nominal flow conditions at the measurement location were: $U_\infty = 12 \text{ m/s}$, $\delta_{99} = 36 \text{ mm}$, $Re_\tau = 1070$. The friction velocity was computed using the Clauser chart method (Clauser, 1954). The mean flow and turbulence statistics showed overall good agreement with Laser Doppler Anemometry (LDA) measurements of similar Reynolds numbers from De Graaff and Eaton (2000).

RESULTS

Large magnitude beam deflections

The simultaneous PIV and MP measurements allow for the use of the MP signal as a condition on which the velocity fields can be averaged. Any scalar quantity q can be conditionally averaged on large positive (downstream) or negative (upstream) MP angle fluctuations, $\theta(t)$: $q|_\theta = \langle q \rangle_{|\theta| > w\sigma_\theta}$, where σ_θ is the standard deviation of the fluctuating MP signal and w is a threshold value, here chosen as $w = 0.5$. Different values of w have been tested and although the exact quantitative results varied, the main trends discussed here were unaltered. In what follows, quantities with the subscript θ will denote averaging on a large MP deflection, the sign of which will be explicitly stated.

In line with the observations from Saxton-Fox *et al.* (2019), both fluctuating velocity fields, when conditioned on large beam deflections show a change in sign across the MP measurement location, that extends across the full boundary layer height (figures 2a and 2b). The sign of the MP deflection (and therefore of the streamwise scalar gradient) matches that of the streamwise velocity gradient (figure 2c), supporting the strong correlation of the two fields when Pr number is close to unity, while the wall-normal velocity gradient is of the opposite sign and is shown to be stronger and more robust across δ (figure 2d). It is also interesting to note that, while the vertical velocity gradient is homogeneous across y , the streamwise velocity gradient shows a

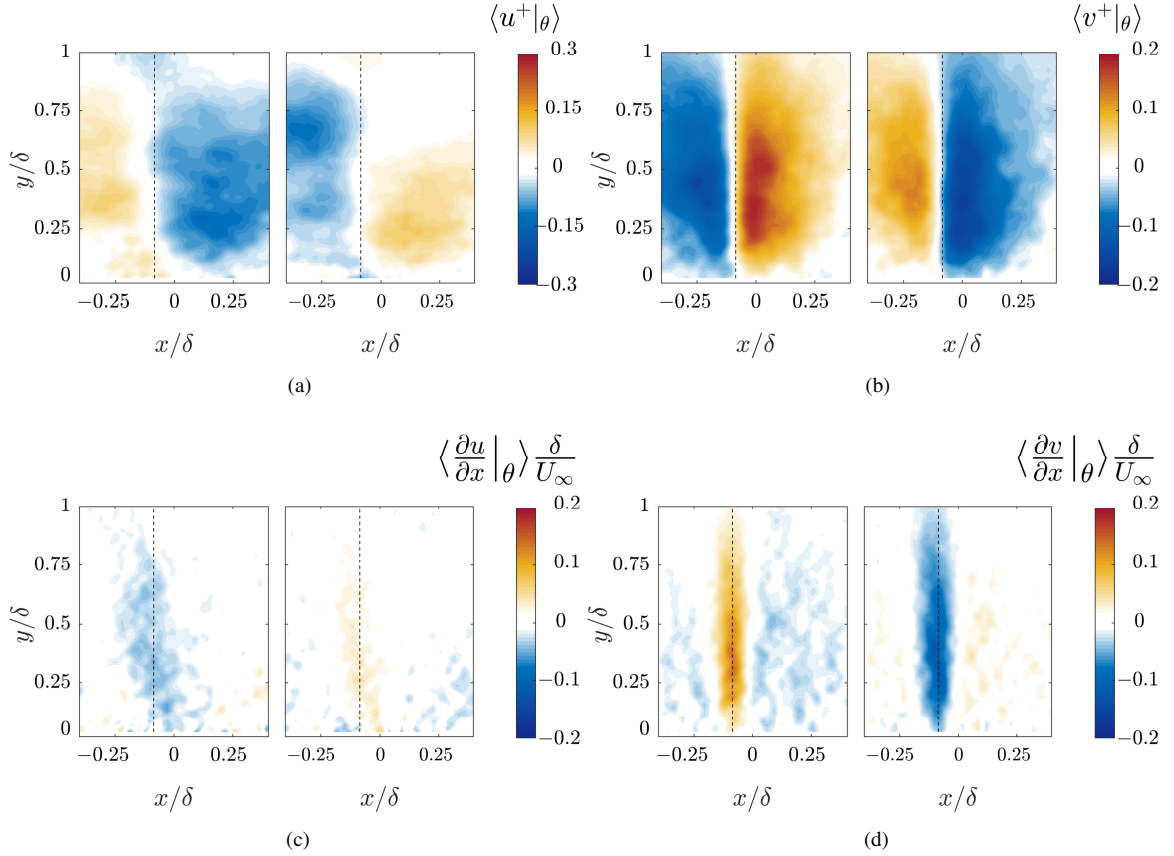


Figure 2. Contour plots of inner-normalised velocity fluctuations and their outer-normalised streamwise gradients, conditionally averaged on the MP deflection angle (negative deflection on the left and positive on the right for all sub-figures). Black dashed lines indicate the MP location. Streamwise velocity fluctuations (a), and the corresponding streamwise gradient (c). Wall-normal velocity fluctuations (b), and the corresponding streamwise gradient (d).

moderate upstream inclination angle, which will be further explored in the following section.

Wall-normal localisation

The wall-normal coherence of the conditionally averaged fields is much larger than the one observed in the instantaneous realisations, suggesting that it is a result of multiple smaller scale structures, situated at different wall-normal locations across δ (Saxton-Fox *et al.*, 2019). The goal of the present work is to identify such structures and explore their geometry for both the streamwise and wall-normal velocities. Since the wall-normal velocity gradient is shown to be the most homogeneous across y in the conditionally averaged fields (figure 2), we use its wall-normal average $s_1(x) = \left\langle \frac{\partial v}{\partial x} \middle| \theta \right\rangle_y$ (see figure 3a), as a second condition upon which the velocity fields associated with large beam deflections will be further classified. Specifically, we assume that each instantaneous wall-normal velocity gradient field associated with a large beam deflection, $s_{2i} = \frac{\partial v}{\partial x}(x, y)$ (for $i = 1, \dots, N|\theta$, where $N|\theta$ is the number of velocity fields associated with a large beam deflection), will contain, at some y location, a structure with similar streamwise signature as $s_1(x)$. We then proceed to identify the wall-normal location y_c for which the correlation coefficient $\rho_{s_1, s_{2i}}$ is maximum (see figure 3b, equation 2):

$$\rho_{s_1, s_{2i}}(y) = \frac{\text{cov}(s_1, s_{2i})}{\sigma_{s_1} \sigma_{s_{2i}}} \quad (2)$$

with $y_c = \text{argmax} \rho_{s_1, s_{2i}}$.

The probability density function (pdf) of y_c , for a large negative MP deflection, indicates that, in most cases, structures more strongly correlated with the average behaviour described by s_1 , are found at locations close to the middle of the boundary layer, $y \approx 0.5\delta$ (figure 3c). A similar picture emerges for y_c in the case of a large positive MP deflection. The location of maximum correlation y_c , can then be used as a second condition upon which to average the velocity fields, a procedure denoted in what follows with the subscript y_c . In particular, instantaneous velocity fields that are associated with large MP deflections using the first condition outlined above, are classified further based on the location of y_c ; for convergence purposes, 5 regions are considered: $y_c \in [0, 0.2\delta)$, $y_c \in [0.2\delta, 0.4\delta)$, $y_c \in [0.4\delta, 0.6\delta)$, $y_c \in [0.6\delta, 0.8\delta)$, and $y_c \in [0.8\delta, 1.0\delta)$. Using the snapshots classified to each of these regions, the conditional velocity fields $\langle u^+ | \theta, y_c \rangle$, and $\langle v^+ | \theta, y_c \rangle$ are computed, using a moving frame of reference; the streamwise axis is unaltered from the one at the Cartesian coordinate system, while the wall-normal one is centred at y_c . Thus, at each streamwise location x , u and v profiles are collected along $y - y_c$, irrespective of the value of y_c within each of the regions chosen. As such, the resulting fields highlight the velocity variation across y_c , and their wall-normal extent is independent of the size of the regions chosen (figure 4).

Results indicate that wall-normal velocity structures that instantaneously exhibit the strongest correlation with the av-

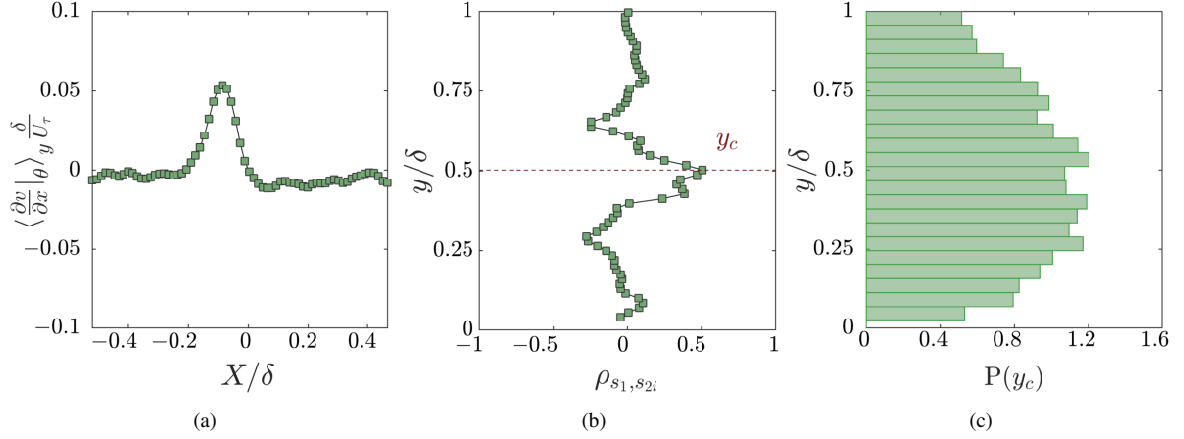


Figure 3. (a) Wall-normal average of the gradient field from figure 2d for a negative MP deflection. (b) Instantaneous example of the wall-normal variation of the correlation coefficient ρ_{s_1, s_2} , where $y_c = \operatorname{argmax} \rho_{s_1, s_2}$. (c) Probability density function of y_c for a negative MP deflection.

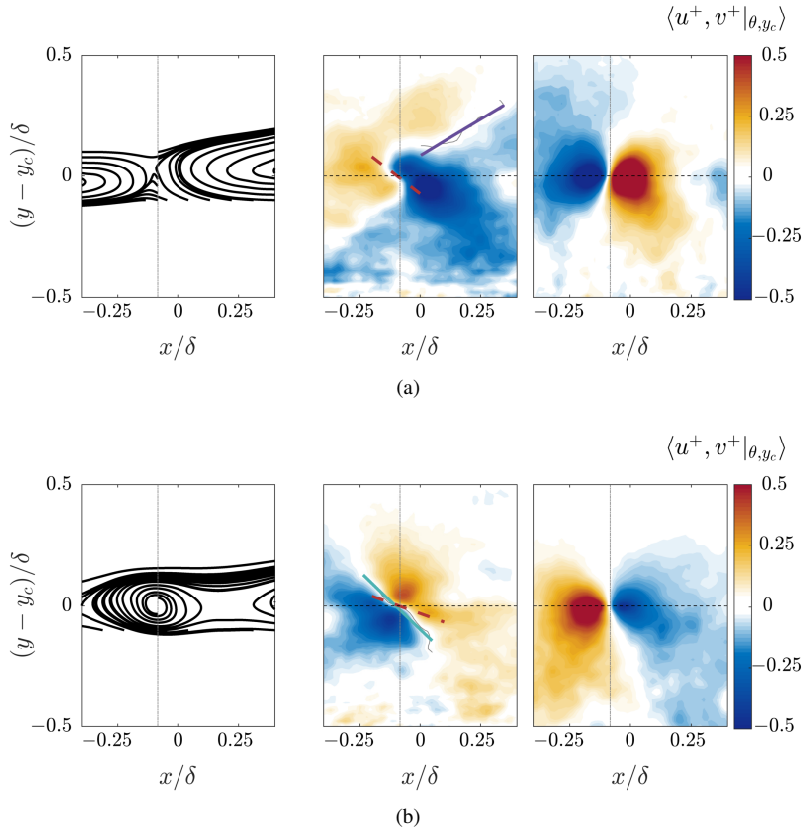


Figure 4. Contour plots of inner-normalised velocity fluctuations, conditionally averaged on both the MP deflection angle and on y_c : $y_c \in [0.4\delta, 0.6\delta]$. (a) Negative MP deflection. (b) Positive MP deflection. The three panels from left to right denote: flow streamlines using the full velocity fields and subtracting $U_c = \langle U(x, y_{cm}) \rangle_x$, streamwise and wall-normal velocity fluctuations, respectively. Vertical solid lines indicate the MP location and horizontal dashed lines $y = y_c$. Red dashed lines indicate the tangent to the $\langle u^+ | \theta, y_c \rangle = 0$ contour at the MP location. Purple and cyan solid lines denote the region of the $\langle u^+ | \theta, y_c \rangle = 0$ contour that is linearly approximated for a negative and positive MP deflection, respectively.

erage behaviour (in terms of the wall-normal velocity gradient) are localised in y . The emerging picture is that of a pair of elliptical v structures of opposing signs (depending on the underlying density gradient) on either side of the MP location (figure 4 for $y_c \in [0.4\delta, 0.6\delta]$). Using an elliptical fit to approximate their extent at 50% of the peak magnitude (figure 5a), reveals a minimal variation in size across all wall-normal locations, with a wall-normal extent

of $\sim 0.1\delta$ (figure 5b). For contours at lower magnitudes, there is a more noticeable size variation, mainly for the regions close to the wall and the freestream.

Regarding the streamwise velocity field, the conditional structures leading to the average behaviour (see figure 2a), are shown to exhibit the expected sign change across the MP location, consistent with the sign of the underlying

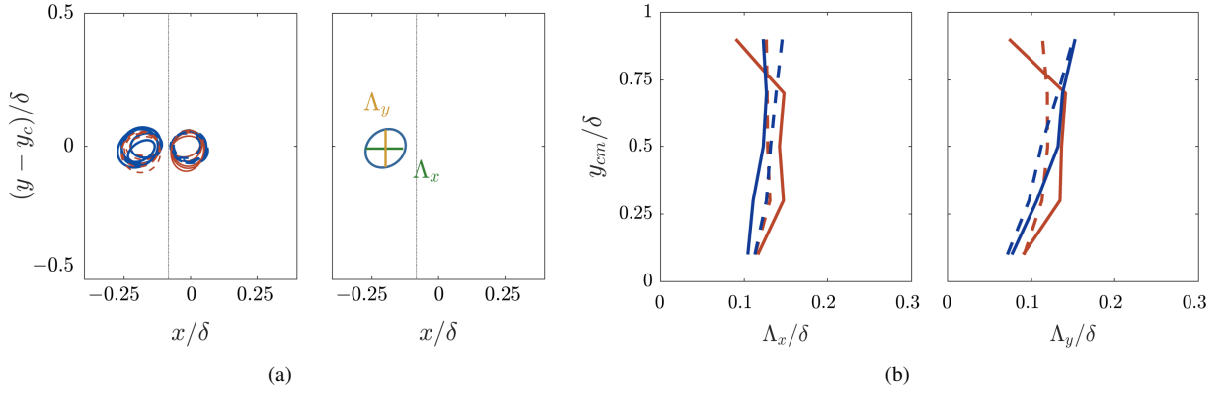


Figure 5. Geometrical characteristics for $\langle v^+ |_{\theta, y_c} \rangle$ (see figure 5) (a) Elliptical fits for the conditionally averaged wall-normal velocity fluctuation contours from figure 5 at 50% of the peak magnitude and for all y_c locations: $y_c \in [0, 0.2\delta]$, $y_c \in [0.2\delta, 0.4\delta]$, $y_c \in [0.4\delta, 0.6\delta]$, $y_c \in [0.6\delta, 0.8\delta]$, and $y_c \in [0.8\delta, 1.0\delta]$. Λ_x and Λ_y denote the streamwise and wall-normal extent respectively. (b) Variation of Λ_x and Λ_y with wall-normal location. Solid lines denote the negative MP deflection (figure 5a) and dashed the positive (figure 5b).

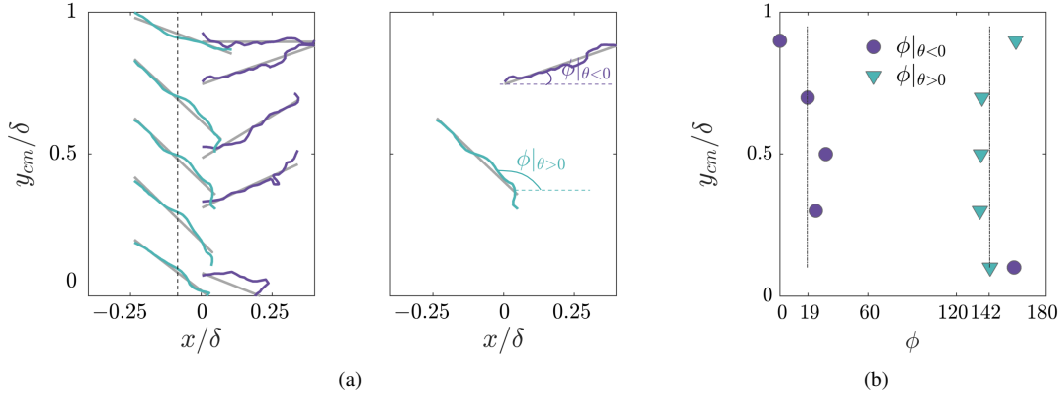


Figure 6. Geometrical characteristics for $\langle u^+ |_{\theta, y_c} \rangle$ (see figure 5). (a) Coloured lines indicate contours of $\langle u^+ |_{\theta, y_c} \rangle = 0$ at all wall-normal locations and grey solid lines denote the linear fits (left). For a positive MP deflection, contours are limited in the streamwise region: $x \in [-0.25\delta, 0.1\delta]$, where $\phi |_{\theta > 0}$ is defined (right). For a negative MP deflection, this region is $x \in [0, 0.4\delta]$, where $\phi |_{\theta < 0}$ is defined. (b) Variation of $\phi |_{\theta < 0}$ and $\phi |_{\theta > 0}$ with wall-normal location.

density gradient. Interestingly, this happens across an upstream leaning interface as indicated by the tangent to the $\langle u^+ |_{\theta, y_c} \rangle = 0$ contour at the MP location (dashed red lines in figure 5, middle panels). This suggests that out of the two possible scenarios outlined earlier (see figure 1) the most prominent geometry associated with a large MP deflection is that of an upstream leaning front. The average behaviour, across all y locations, of the streamwise velocity gradient, hinted at that (see figure 2c), although the effect was significantly suppressed. For large negative MP deflections, this upstream slope is fairly narrow, centred around the MP location, and it is seen to be imposed on a larger-scale, downstream leaning $\langle u^+ |_{\theta, y_c} \rangle = 0$ contour creating a sawtooth profile. A linear fit of this downstream leaning contour (solid purple line in figure 5, middle panel, top row) results in an angle $\phi |_{\theta < 0} \sim 18^\circ$, for $y_c \in [0.2\delta, 1.0\delta]$ (figure 6). Close to the wall, this larger-scale, downstream leaning interface is much less pronounced and $\phi |_{\theta < 0}$ approaches 180° (figure 6b). For large positive MP deflections, the larger-scale structure is absent and the upstream leaning $\langle u^+ |_{\theta, y_c} \rangle = 0$ contour dominates the conditional structure across x (solid cyan line in figure 5, middle panel, bottom row) at an average angle $\phi |_{\theta > 0} \sim 142^\circ$, almost constant throughout the boundary layer (figure 6b).

Finally, the addition of the mean flow field \bar{U} , and the subtraction of a constant convection velocity allows the analysis of the flow topology associated with these conditional velocity fluctuations, at each region of y_c . For a convection velocity U_c , equal to the mean velocity at the middle of each region y_{cm} , the resulting streamlines highlight the presence of a saddle point for the case of a negative MP deflection and a focus point in the case of a positive deflection (left panels in figures 4a and 4b), a behaviour consistent throughout the boundary layer. The same critical point behaviour was observed by Antonia and Fulachier (1989) who used concurrent temperature and velocity measurements from cold-wire and hot-wire anemometry respectively, and analysed the flow topology conditioned on the presence of strong negative (coolings) and positive (heatings) temperature gradients in time. Taking into account the relationship between temperature and density in an ideal gas and the analogy between density gradients and the measured MP angle (equation 1), we can conclude that heatings in time would be consistent with strong positive MP deflections (positive streamwise density gradients), while coolings could be identified with negative MP deflections (negative streamwise density gradients). Although there are several differences between the two measurement techniques,

the strong similarities in the resulting flow topologies support the assumption that the underlying flow structures giving rise to strong aero-optic distortions of a certain orientation, and to temperature gradients of a certain sign are closely connected. This could allow more direct comparisons of the current technique with the existing vast body of work employing cold wire measurements.

DISCUSSIONS AND CONCLUSIONS

Simultaneous particle image velocimetry and Malley probe (MP) measurements were performed in a moderately heated turbulent boundary layer. Velocity fluctuations conditioned on large MP deflections revealed a clear change in sign for both u and v velocities, consistent throughout the boundary layer height. In an effort to determine which scales contributed to this average behaviour, structures that instantaneously were more strongly correlated with the average behaviour were identified and were shown to be localised in y . The v fluctuations exhibited an average wall-normal extent $\sim 0.1\delta$ almost constant across y , in line with the conceptual model introduced by Saxton-Fox *et al.* (2019), where the tall, conditionally averaged v structures (figure 2b), were a result of a superposition of smaller-scale v events, sitting at different heights from the wall (figure 7). The condi-

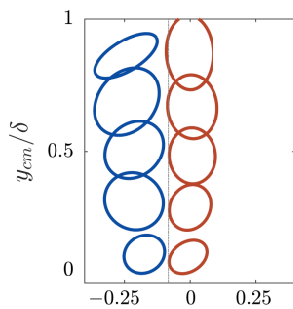


Figure 7. Contours of inner-normalised vertical velocity fluctuations at 30% of their peak magnitude, conditionally averaged on both a negative MP deflection and on y_c , supporting the conceptual schematic proposed by Saxton-Fox *et al.* (2019).

tional u structures revealed a sign change across upstream leaning interfaces—more prominent for positive MP deflections. The resulting flow topology supported results by Antonia and Fulachier (1989), enabling more direct comparisons with cold-wire studies. The emerging picture from the conditional fields of both the streamwise and wall-normal velocity fluctuations is consistent with earlier ideas of temperature ramps with a sawtooth profile (Gibson *et al.*, 1977) and of ‘typical eddies’ superimposed on turbulent bulges (Falco, 1977), while it also supports recent low-order modelling results of passive scalar transport, based on a superposition of different velocity scales (Saxton-Fox *et al.*, 2019). Future work aims to exploit the available time information from the MP signal and extend the current structural analysis leveraging observations from cold-wire studies in order to allow for a more complete conceptual picture and inform further modelling efforts.

ACKNOWLEDGEMENTS

This work was supported by the ONR under grant number N00014-17-1-3022.

REFERENCES

- Abe, H., Antonia, R.A. and Kawamura, H. 2009 Correlation between small-scale velocity and scalar fluctuations in a turbulent channel flow. *Journal of Fluid Mechanics* **627**, 1–32.
- Antonia, R.A., Abe, H. and Kawamura, H. 2009 Analogy between velocity and scalar fields in a turbulent channel flow. *Journal of Fluid Mechanics* **628**, 241–268.
- Antonia, R. A. and Fulachier, L. 1989 Topology of a turbulent boundary layer with and without wall suction. *Journal of Fluid Mechanics* **198**, 429–451.
- Bisset, D. K., Antonia, R. A. and Raupach, M. R. 1991 Topology and transport properties of large scale organized motion in a slightly heated rough wall boundary layer. *Physics of Fluids A: Fluid Dynamics* **3** (9), 2220–2228.
- Chen, C-H. P. and Blackwelder, R. F. 1978 Large-scale motion in a turbulent boundary layer: a study using temperature contamination. *Journal of Fluid Mechanics* **89**, 1–31.
- Clauser, Francis H 1954 Turbulent boundary layers in adverse pressure gradients. *Journal of the Aeronautical Sciences* **21** (2), 91–108.
- De Graaff, D. B. and Eaton, J. K. 2000 Reynolds-number scaling of the flat-plate turbulent boundary layer. *Journal of Fluid Mechanics* **422**, 319–346.
- Falco, R.E. 1977 Coherent motions in the outer region of turbulent boundary layers. *Physics of Fluids* **20** (10), S124–S132.
- Fulachier, L. and Dumas, R. 1976 Spectral analogy between temperature and velocity fluctuations in a turbulent boundary layer. *Journal of Fluid Mechanics* **77** (2), 257–277.
- Gibson, C.H., Friehe, C.A. and McConnell, S.O. 1977 Structure of sheared turbulent fields. *The Physics of Fluids* **20** (10), S156–S167.
- Gladstone, J. H. and Dale, T. P. 1862 Researches on the refraction, dispersion, and sensitiveness of liquids. *Proceedings of the Royal Society of London* **12**, 448–453.
- Gordeyev, S., Cress, J.A., Smith, A.E. and Jumper, E.J. 2015 Aero-optical measurements in a subsonic, turbulent boundary layer with non-adiabatic walls. *Physics of Fluids* **27** (4), 045110.
- Gordeyev, S., Smith, A. E., Cress, J. and Jumper, E.J. 2014 Experimental studies of aero-optical properties of subsonic turbulent boundary layers. *Journal of Fluid Mechanics* **740**, 214–253.
- Malley, M.M., Sutton, G.W. and Kincheloe, N. 1992 Beam-jitter measurements of turbulent aero-optical path differences. *Applied Optics* **31**, 4440–4443.
- Saxton-Fox, T., McKeon, B.J. and Gordeyev, S. 2019 Effect of coherent structures on aero-optic distortion in a heated turbulent boundary layer. *AIAA Journal* pp. 1–12.
- Saxton-Fox, T. and McKeon, B. J. 2017 Modeling momentum and scalar transport in a wall-bounded turbulent flow. In *TSFP Digital Library Online*. Chicago, IL.